Supplementary Information (SI) for Journal of Materials Chemistry C.

Controlling self-assembly and charge transport in photo-responsive nanostructured materials

Yu Cao,*[a,b] Tejal Nirgude,[c] Frédéric Dubois,[d] Dharmendra Pratap Singh,*[d] Fengcheng Xi,[a] Feng Liu,[a,b,] Mohamed Alaasar*[c,e]

[a]*Shaanxi International Research Center for Soft Matter, State Key Laboratory for Mechanical Behavior of Materials, Xi'an Jiaotong University, Xi'an 710049, P. R. China*
[b]*Institute of New Concept Sensors and Molecular Materials, Shaanxi Key Laboratory of New Concept Sensors and Molecular Materials, Xi'an Jiaotong University, Xi'an, 710049 P. R. China*
[c]*Institute of Chemistry, Martin Luther University Halle-Wittenberg, 06120 Halle, Germany*
[d]*UDSMM, Unité de Dynamique et Structure des Matériaux Moléculaires, Université du Littoral Côte d'Opale, UR 4476, Calais F-62228, France*
[e]*Department of Chemistry, Faculty of Science, Cairo University, 12613 Giza, Egypt*

Contents

1. Methods

Optical and calorimetric investigations. Phase transitions were determined by polarizing microscopy (Leica DMR XP) in conjunction with a heating stage (FP 82 HT, Mettler) and controller (FP 90, Mettler) and by differential scanning calorimetry (DSC-7, Perkin Elmer) at heating/cooling rates of 10 K min^{-1} (peak temperatures). Optical investigation was carried out under equilibrium conditions between glass slides, which were used without further treatment, sample thickness was ~15 μm. A full wavelength retardation plate was used to determine the sign of birefringence. Optical micrographs were taken using a Leica MC120HD camera.

High-resolution small-angle X-ray scattering. SAXS experiments were recorded on Beamline BL16B1 at the Shanghai Synchrotron Radiation Facility (SSRF). Samples were held in evacuated 1 mm capillaries. A modified Linkam hot stage with thermal stability within 0.2 ºC was used, with a hole for the capillary drilled through the silver heating block and mica windows attached to it on each side. A Pilatus 2M detector was used. q Calibration and linearization were verified using several orders of layer reflections from silver behenate and a series of *n*-alkanes. Experimental diffractograms are fitted using Gaussian-shaped peaks to determine the positions and intensities of the diffraction peaks. The diffraction peaks are indexed based on their peak positions, and the lattice parameters and the space groups are subsequently determined.

Once the diffraction intensities are measured and the corresponding plane group determined, 3D electron density maps can be reconstructed based on the general formula.

$$E(xyz) = \sum_{hkl} F(hkl)\, e^{[i2\pi(hx+ky+lz)]} \quad (1)$$

Here, $F(hkl)$ is the structure factor of a diffraction peak with index (hkl). It is normally a complex number, and the experimentally observed diffraction intensity is

$$I(xyz) = K \cdot F(hkl) = F*(hkl) = K \cdot |F(hkl)|^2 \quad (2)$$

Here, K is a constant related to the sample volume, incident beam intensity etc. If the constant is equal to 1, then the electron density is

$$E(xyz) = \sum_{hkl} \sqrt{I(hkl)}\, e^{[i2\pi(hx+ky+lz)+\Phi_{hkl}]} \quad (3)$$

As the observed diffraction intensity, $I(hkl)$, is only related to the amplitude of the structure factor $|F(hkl)|$, the information about the phase of $F(hkl)$, Φ_{hkl}, cannot be determined directly from the experiment. However, the problem is much simplified when the structure of the

ordered phase is centrosymmetric; hence, the structure factor $F(hkl)$ is always real, and Φ_{hkl} is either 0 or π.

This makes it possible for a trial-and-error approach, where candidate electron density maps are reconstructed for all possible phase combinations. The "correct" phase combination is then selected on the merit of the maps, helped by prior physical and chemical knowledge of the system. This is especially useful for studying nanostructures, where typically only a limited number of diffraction peaks are observed.

2. Synthesis

2.1. Purification and analytical methods

Thin-layer chromatography (TLC) was performed on an aluminium sheet precoated with silica gel. Analytical quality chemicals were obtained from commercial sources and used as obtained. The solvents were dried using the standard methods when required. The purity and the chemical structures of all compounds synthesized were confirmed by the spectral data. The structure characterization of the synthesized bent-core compounds is based on ^{1}H-NMR, ^{13}C-NMR, and ^{19}F-NMR (Agilent Technologies 400 MHz VNMRS and 500 MHz DD2 spectrometers, in $CDCl_3$ solution. ^{1}H-NMR and ^{13}C-NMR chemical shifts are reported in ppm referenced to tetramethylsilane. The residual proton signal of the deuterated solvent was used as an internal standard for ^{1}H NMR and ^{13}C-NMR spectra. ^{19}F NMR chemical shifts are reported in ppm referenced to trichlorofluoromethane as an external standard. Mass analyses were performed using a Bruker micrOTOF-Q II APPI HRMS-High Resolution Mass Spectrometer.

2.2. Synthesis and analytical data

2.2.1. Synthesis of **2**:

4-Formylbenzoic acid (0.30 mmol, 330 mg), 2-benzoyloxy-4-bromoresorcinol **1**[S1] (0.30 mmol, 600 mg), and a catalytic amount of DMAP were dissolved in dichloromethane with stirring. After 10 minutes, DCC (0.33 mmol, 690 mg) previously dissolved in dichloromethane (DCM) was added to the reaction mixture, and stirring was continued for 24 hours. The reaction progress was checked with TLC, and at the end of the reaction, the formed white solid was filtered out and washed three times with DCM. The solvent was then removed under vacuum, and the crude material obtained was purified with column chromatography using DCM to give the desired material as a pale-yellow oil.

2. Pale yellow oil, yield 82.81%. ^{1}H NMR (400 MHz, $CDCl_3$) δ 10.15 (s, 1H, Ar-CHO), 8.34 (d, 2H, Ar-H), 8.03 (d, 2H, Ar-H), 7.62 (d, *J* = 8.6 Hz, 1H, Ar-H), 7.51 – 7.29 (m, 5H, Ar-H), 6.89 (d, *J* = 2.5 Hz, 1H, Ar-H), 6.78 (dd, *J* = 8.6, 2.5, 0.6 Hz, 1H, Ar-H), 5.16 (s, 2H, Ar-O$\underline{CH_2}$Ph).

2.2.2. Synthesis of **3**:

The aldehyde **2** was oxidized to the corresponding acid **3** using a similar method to that reported in Ref. [S1] as follows: the aldehyde **2** (2.23 mmol, 920 mg) and resorcinol (1.2 mmol, 132 mg) were dissolved in *tert*-butanol (50 mL). To this solution, sodium chlorite (3.4 mmol, 307 mg) and sodium dihydrogenphosphate (2.1 mmol, 408 mg) dissolved in water (10 mL) were added dropwise over 10 minutes. The reaction mixture was then stirred at room temperature overnight. The solution was concentrated under vacuum, and the residue was dissolved in water (100 mL) and acidified to pH 3 with 1 N aqueous HCl. The obtained white precipitate was filtered off and washed successively with water and hexane and dried in air. The obtained acid **3** was used for the next step without the need for any further purification.

3. White powder, yield 97%. ^{1}H NMR (400 MHz, DMSO-d_6) δ 8.22 (d, 2H, Ar-H), 8.13 (d, 2H, Ar-H), 7.68 (d, *J* = 8.6 Hz, 1H, Ar-H), 7.50 – 7.30 (m, 5H, Ar-H), 7.29 (d, *J* = 2.5 Hz, 1H, Ar-H), 6.91 (dd, *J* = 8.6, 2.5 Hz, 1H, Ar-H), 5.19 (s, 2H, Ar-O$\underline{CH_2}$Ph).

2.2.3. Synthesis of **4**:

3,4,5-Tri-*n*-hexadecyloxybenzoic acid [S2] (2.8 g, 3.33 mmol) was heated under reflux with excess thionyl chloride (5 mL) and a catalytic amount of *N*, *N*-dimethylformamide (DMF) for one hour. The excess thionyl chloride was removed under reduced pressure, followed by the addition of 4,4'-dihydroxybiphenyl (3.1 g, 16.66 mmol) dissolved in dry pyridine (75 mL), and the mixture was heated at 60 °C for 24 hours with stirring. After cooling the solution to room temperature, it was poured into ice and acidified with HCl. The obtained white solid was filtered off, washed several times with water, and purified by column chromatography using dichloromethane as an eluent to give the desired material as a white powder. Yield 44.40% (wt = 1.49 g), m.p.~ 74-76 °C. ^{1}H NMR (400 MHz, $CDCl_3$) δ 7.57 (d, 2H, Ar-H), 7.47 (d, *J* = 8.7, 2.3 Hz, 2H, Ar-H), 7.43 (s, 2H, Ar-H), 7.30 – 7.19 (m, 2H, Ar-H), 6.90 (d, 2H, Ar-H), 5.30 (s, 1H, Ar-OH), 4.18 – 3.91 (m, 6H, Ar-O$\underline{CH_2}$), 1.98 – 1.66 (m, 6H, Ar-OCH$_2\underline{CH_2}$), 1.65 – 1.05 (m, 78H, 39 X CH_2), 0.98 – 0.77 (m, 9H, 3 X CH_3).

2.2.4. Synthesis of **6**:

The acid **3** (1.0 mmol, 0.43 g) was converted to the corresponding acid chloride using the method described above for 3,4,5-tri-*n*-hexadecyloxybenzoyl chloride. The acid chloride was then dissolved in dry dichloromethane (DCM, 20 mL), and the corresponding hydroxy compound **5** (1.0 mmol, 1.0 g),[S3] previously dissolved in DCM (10 mL) was added, followed by the addition of triethylamine (TEA, 1.2 mmol, 0.12 g) and a catalytic amount of dry pyridine. The solution was then refluxed for 6 hours under an argon atmosphere. At the end of the reaction, the solution was cooled to room temperature and washed with 10% HCl (2 × 50 mL) and several times with cold water, then extracted with DCM (3 × 50 mL) and finally dried over anhydrous sodium sulphate. After removing the solvent, the crude material was chromatographed on silica gel using dichloromethane.

6. White solid, 1.10 g, Yield 76.97%. Column from $CHCl_3$: *n*-Hexane (3:1). M.p. ~ 118-120 °C. ^{1}H NMR (400 MHz, $CDCl_3$) δ 8.42 – 8.27 (m, 4H, Ar-H), 7.73 – 7.59 (m, 5H, Ar-H), 7.52 – 7.46 (m, 2H, Ar-H), 7.46 – 7.27 (m, 9H, Ar-H), 6.92 (d, *J* = 2.5 Hz, 1H, Ar-H), 6.81 (dd, *J* = 8.5, 2.5 Hz, 1H, Ar-H), 5.17 (s, 2H, Ar-O$\underline{CH_2}$Ph), 4.19-3.98 (m, 6H, Ar-O$\underline{CH_2}CH_2$), 1.92 – 1.66 (m, 6H, Ar-O$CH_2\underline{CH_2}$), 1.61 – 1.09 (m, 78H, 39 X CH_2), 0.98 – 0.76 (m, 9H, 3 X CH_3).

2.2.5. Synthesis of **7**:

A suspension of compound **6** (0.7 mmol, 0.95 g) and Pd/C (10% Pd, 0.3 g) in 80 mL THF was flushed with hydrogen. The mixture was stirred at room temperature at normal pressure for 24 hours. The solid material was removed by filtration, and the solvent was evaporated under reduced pressure. The crude white product was purified by recrystallization from methanol to give the desired material as white crystals. 0.59 g, Yield 66.31%. ^{1}H NMR (400 MHz, $CDCl_3$) δ 8.43 – 8.30 (m, 4H, Ar-H), 7.77 – 7.59 (m, 4H, Ar-H), 7.53 (d, *J* = 8.7 Hz, 1H, Ar-H), 7.43 (s, 2H, Ar-H), 7.39 – 7.27 (m, 4H, Ar-H), 6.84 (dd, *J* = 8.3, 2.0 Hz, 1H, Ar-H), 6.81 – 6.73 (m, 1H, Ar-H), 5.65 (s, 1H, Ar-OH), 4.16 – 3.97 (m, 6H, Ar-O$\underline{CH_2}CH_2$), 1.94 – 1.69 (m, 6H, Ar-O$CH_2\underline{CH_2}$), 1.67 – 1.14 (m, 78H, 39 X CH_2), 0.98 – 0.77 (m, 9H, 3 X CH_3).

2.2.6. Synthesis of final compounds:

General Procedure. The azobenzene-based benzoic acid derivatives (**8XY**)[S4] (1.0 mmol) were converted to the corresponding acid chloride as described above. To the obtained acid chloride, the hydroxy compound **7** (1 equivalent) dissolved in 25 mL of dry dichloromethane was added together with triethylamine (1.2 equivalents) and a catalytic amount of pyridine. The

reaction mixture was refluxed for 6 hours. The crude product was extracted with dichloromethane (3 X 50 mL). The obtained organic layer was washed twice with water and dried over anhydrous $MgSO_4$, and the solvent was removed under reduced pressure. The resulting orange solid material was chromatographed in a silica column using CH_2Cl_2, followed by recrystallization from an ethanol/chloroform mixture (4/1) to give the final compounds as orange crystals.

AHH. Orange powder. 70 mg, Yield 54.09%. **^{1}H NMR** (502 MHz, $CDCl_3$) δ 8.45 – 8.27 (m, 6H, Ar-H), 8.03 – 7.94 (m, 4H, Ar-H), 7.75 (d, *J* = 8.7 Hz, 1H, Ar-H), 7.71 – 7.59 (m, 4H, Ar-H), 7.43 (s, 2H, Ar-H), 7.39 – 7.31 (m, 3H, Ar-H), 7.32 – 7.26 (m, 2H, Ar-H overlapped with $CHCl_3$), 7.17 (dd, *J* = 8.7, 2.6 Hz, 1H, Ar-H), 7.07 – 6.98 (m, 2H, Ar-H), 4.13 – 4.00 (m, 8H, Ar-O$\underline{CH_2}$-), 1.96 – 1.68 (m, 8H, Ar-OCH$_2\underline{CH_2}$-), 1.65 – 1.13 (m, 96H, 48 X $\underline{CH_2}$), 0.97 – 0.77 (m, 12H, 4 X $\underline{CH_3}$). **^{13}C NMR** (126 MHz, $CDCl_3$) δ 165.22, 164.51, 164.07, 162.70, 153.16, 151.69, 150.39, 147.06, 138.73, 138.17, 134.17, 131.43, 130.54, 130.52, 130.18, 128.47, 128.38, 125.49, 123.99, 122.74, 122.33, 122.08, 115.90, 115.02, 108.83, 73.77, 69.49, 68.66, 32.09, 32.08, 30.52, 29.92, 29.90, 29.87, 29.84, 29.83, 29.80, 29.75, 29.72, 29.57, 29.52, 29.50, 29.49, 29.32, 26.26, 26.23, 26.16, 22.85, 14.26. **HRMS:** Calcd. for $C_{106}H_{149}BrN_2O_{12}$ [M^+]: 1721.028, found 1721.027.

AFH. Orange powder. 76 mg, Yield 57.11%. **^{1}H NMR** (502 MHz, $CDCl_3$) δ 8.40 – 8.30 (m, 6H, Ar-H), 7.99 (d, *J* = 8.6 Hz, 2H, Ar-H), 7.83 (d, *J* = 8.6 Hz, 1H, Ar-H), 7.75 (d, *J* = 11.9 Hz, 1H, Ar-H), 7.70 – 7.61 (m, 4H, Ar-H), 7.54 (t, *J* = 8.2 Hz, 1H, Ar-H), 7.43 (s, 2H, Ar-H), 7.39 – 7.31 (m, 3H, Ar-H), 7.31 – 7.20 (m, 3H, Ar-H overlapped with chloroform signal), 7.10 (t, *J* = 8.6 Hz, 1H, Ar-H), 4.14 (t, *J* = 6.6 Hz, 2H, Ar-O$\underline{CH_2}$-), 4.12 – 4.00 (m, 6H, Ar-O$\underline{CH_2}$-), 1.94-1.69 (m, 8H, Ar-OCH$_2\underline{CH_2}$-), 1.60 – 1.16 (m, 96H, 48 X $\underline{CH_2}$), 0.94 – 0.83 (m, 12H, 4 X $\underline{CH_3}$). **^{13}C NMR** (126 MHz, $CDCl_3$) δ 165.22, 164.43, 164.41, 164.06, 155.71, 154.07, 153.16, 152.10, 151.71, 151.65, 151.41, 150.99, 150.82, 150.71, 150.38, 146.66, 146.62, 143.31, 138.72, 138.16, 134.18, 133.86, 131.70, 131.45, 130.67, 130.54, 130.52, 130.19, 128.49, 128.47, 128.41, 128.37, 123.98, 122.91, 122.33, 122.23, 122.08, 122.07, 119.66, 119.35, 115.88, 113.65, 108.83, 108.12, 107.97, 73.76, 69.74, 69.48, 32.09, 32.09, 32.07, 30.52, 30.47, 30.36, 29.93, 29.91, 29.90, 29.87, 29.84, 29.82, 29.80, 29.78, 29.73, 29.69, 29.67, 29.64, 29.56, 29.54, 29.52, 29.50, 29.49, 29.39, 29.22, 26.26, 26.23, 26.19, 26.17, 26.05, 22.84, 14.26. **^{19}F NMR** (473 MHz, $CDCl_3$) δ -132.54 (t, *J* = 9.9 Hz). **HRMS:** Calcd. for $C_{106}H_{148}BrFN_2O_{12}$ [M^+]: 1739.019, found 1739.018.

AFF. Orange powder. 77 mg, Yield 58.24%. ^{1}H NMR (502 MHz, $CDCl_3$) δ 8.44 – 8.30 (m, 6H, Ar-H), 8.04 (d, *J* = 8.6 Hz, 2H, Ar-H), 7.75 (d, *J* = 8.7 Hz, 1H, Ar-H), 7.70 – 7.56 (m, 5H), 7.43 (s, 1H, Ar-H), 7.39 – 7.31 (m, 5H, Ar-H), 7.31 – 7.27 (m, 1H, Ar-H), 7.17 (dd, *J* = 8.7, 2.7 Hz, 1H, Ar-H), 6.83 (ddd, *J* = 9.4, 7.5, 1.8 Hz, 1H, Ar-H), 4.15 (t, *J* = 6.6 Hz, 2H, Ar-O$\underline{CH_2}$-), 4.12 – 4.01 (m, 6H, Ar-O$\underline{CH_2}$-), 1.92 – 1.71 (m, 8H, Ar-OCH$_2\underline{CH_2}$-), 1.65 – 1.15 (m, 96H, 48 X $\underline{CH_2}$), 0.97 – 0.81 (m, 12H, 4 X $\underline{CH_3}$). ^{13}C NMR (126 MHz, $CDCl_3$) δ **^{13}C NMR** (126 MHz, cdcl$_3$) δ 165.22, 164.44, 164.36, 164.07, 155.88, 153.16, 151.62, 151.41, 150.82, 150.38, 143.32, 138.73, 138.17, 134.18, 133.86, 131.47, 131.04, 130.55, 130.52, 130.19, 128.48, 128.38, 123.98, 123.14, 122.33, 122.07, 119.38, 115.88, 112.15, 112.12, 108.84, 108.68, 108.66, 73.77, 70.26, 69.49, 32.09, 32.07, 30.52, 29.91, 29.90, 29.87, 29.84, 29.83, 29.80, 29.78, 29.74, 29.72, 29.67, 29.57, 29.54, 29.52, 29.49, 29.45, 29.21, 26.26, 26.23, 25.98, 22.85, 14.26. **^{19}F NMR** (473 MHz, $CDCl_3$) δ -145.76 – -146.33 (m), -157.75 – -158.36 (m). **HRMS:** Calcd. for $C_{106}H_{147}BrF_2N_2O_{12}$ [M^+]: 1757.010, found 1757.008.

3. NMR Spectra

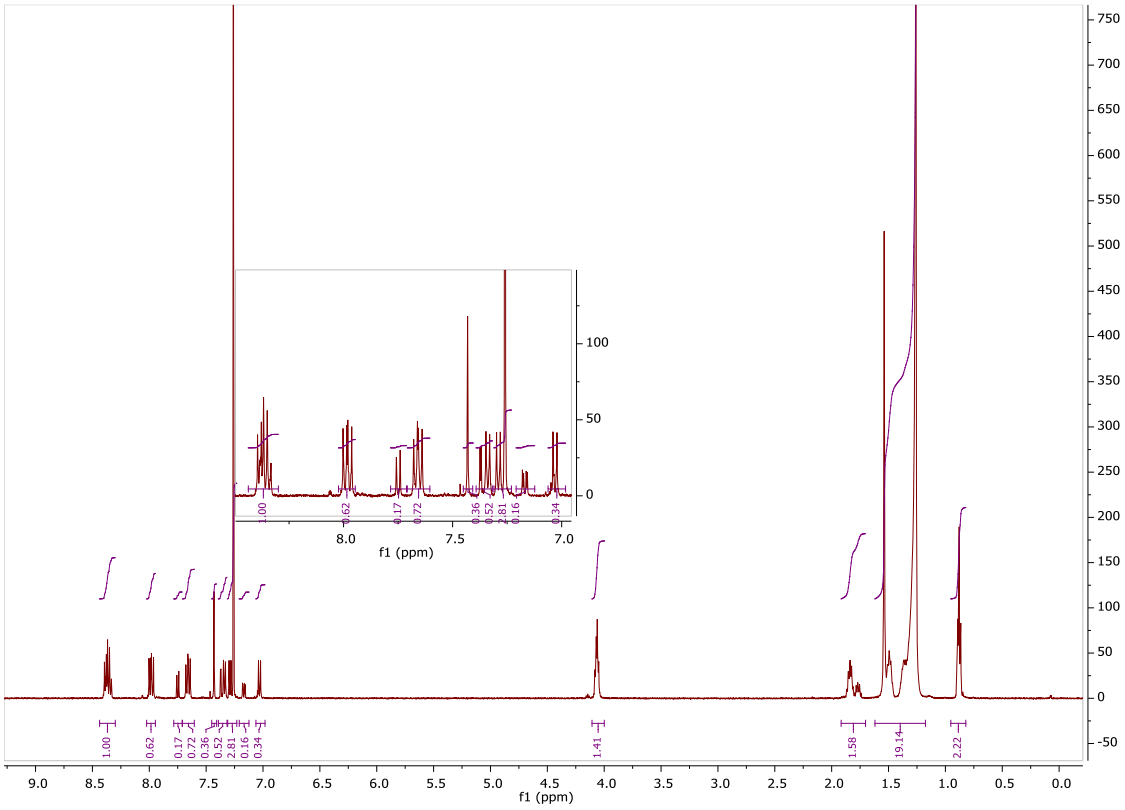

Figure S1. ^{1}H-NMR Spectrum of **AHH** in $CDCl_3$.

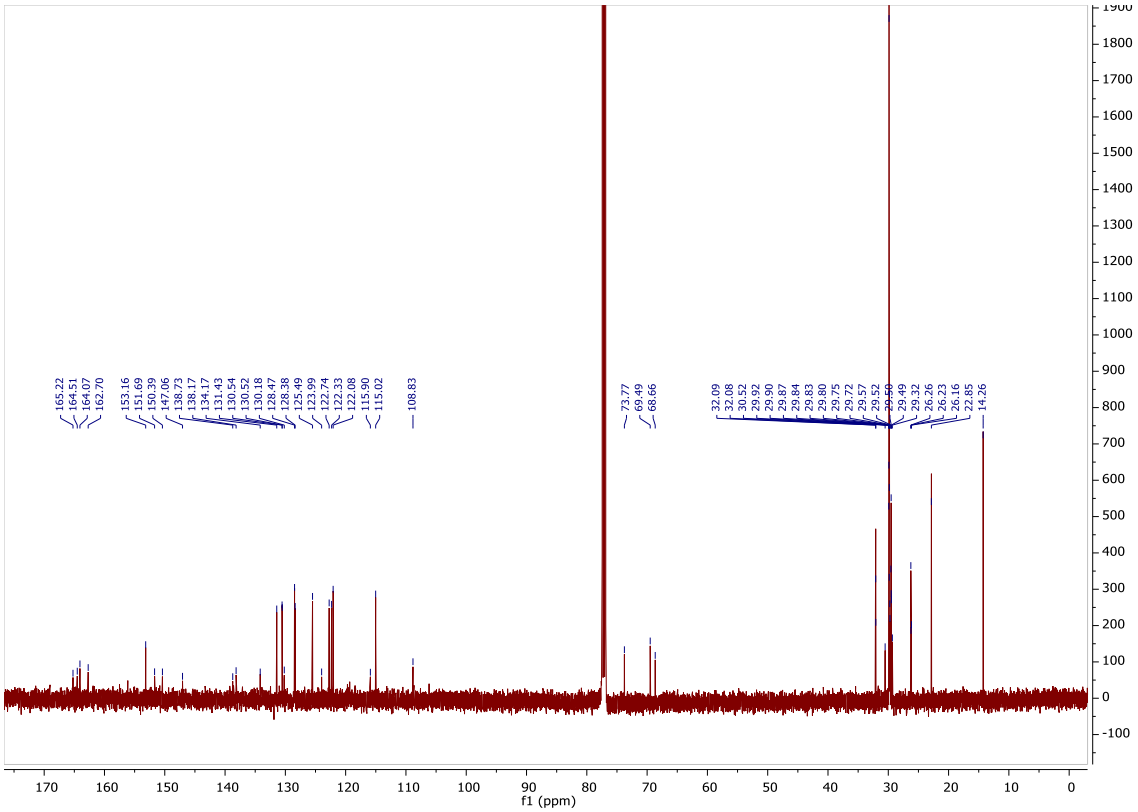

Figure S2. ^{13}C-NMR Spectrum of **AHH** in $CDCl_3$.

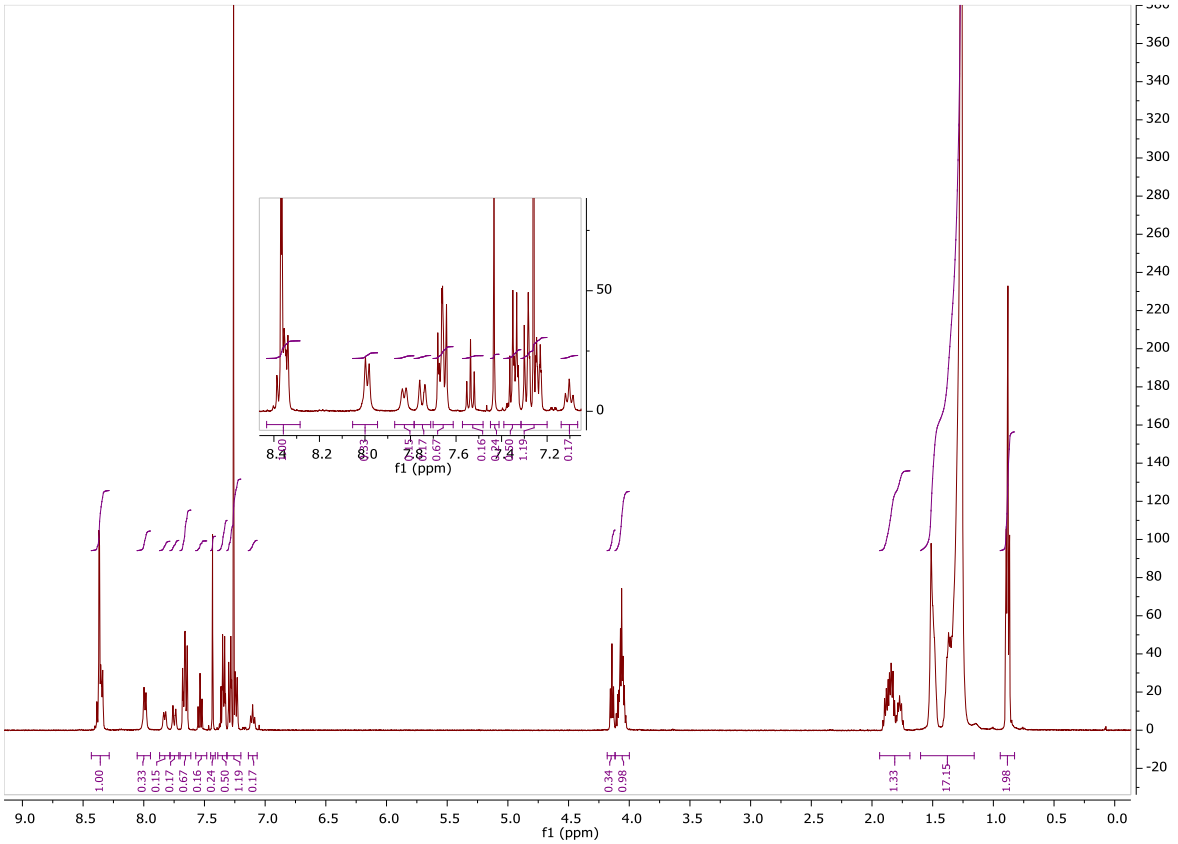

Figure S3. ^{1}H-NMR Spectrum of **AFH** in $CDCl_3$.

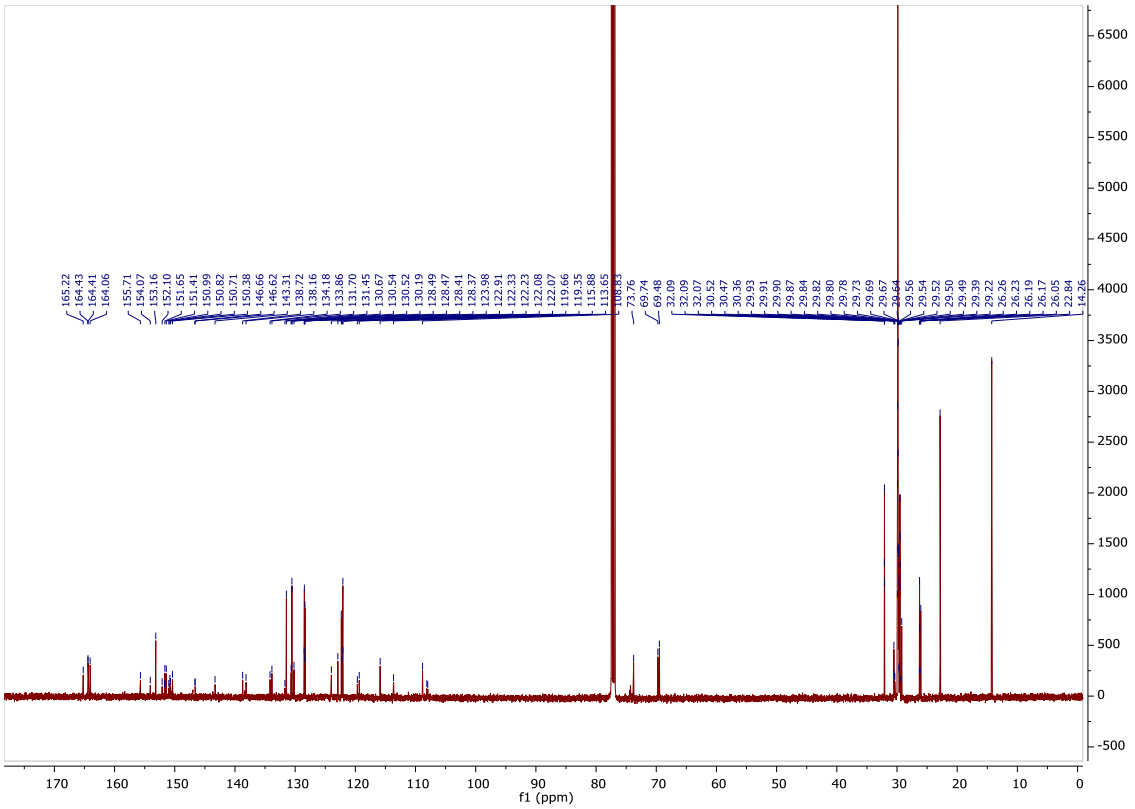

Figure S4. ^{13}C-NMR Spectrum of **AFH** in $CDCl_3$.

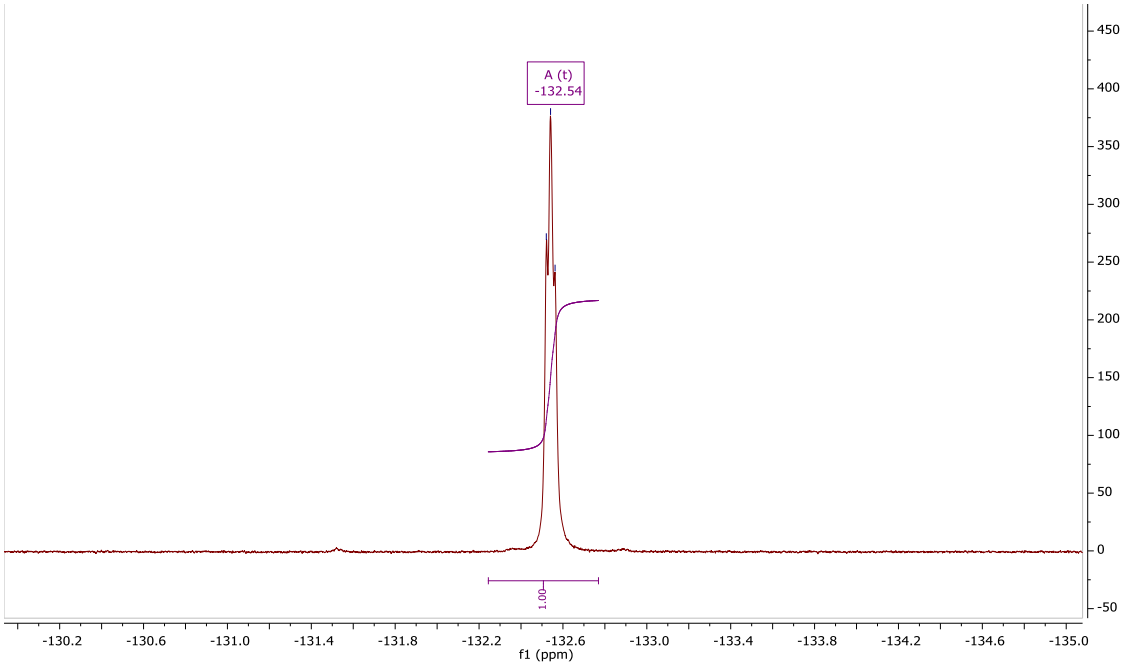

Figure S5. ^{19}F-NMR Spectrum of **AFH** in $CDCl_3$.

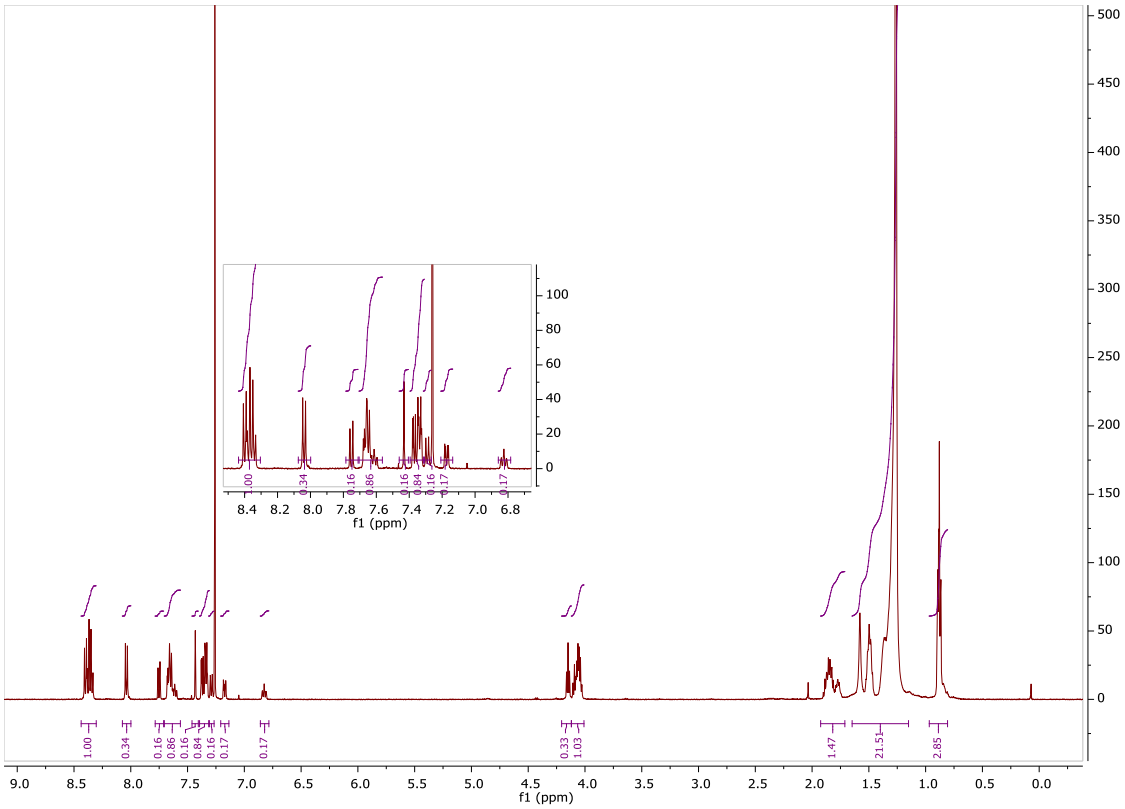

Figure S6. ^{1}H-NMR Spectrum of **AFF** in $CDCl_3$.

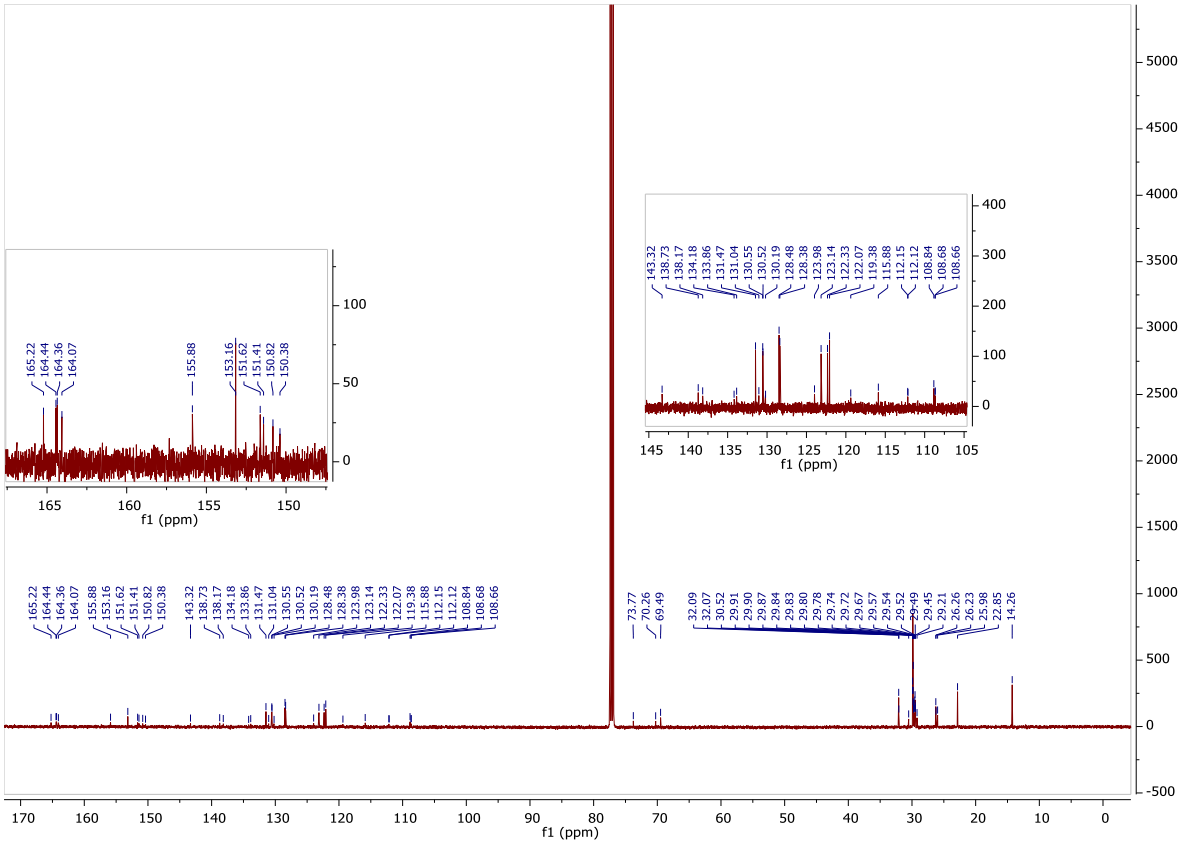

Figure S7. ^{13}C-NMR Spectrum of **AFF** in $CDCl_3$.

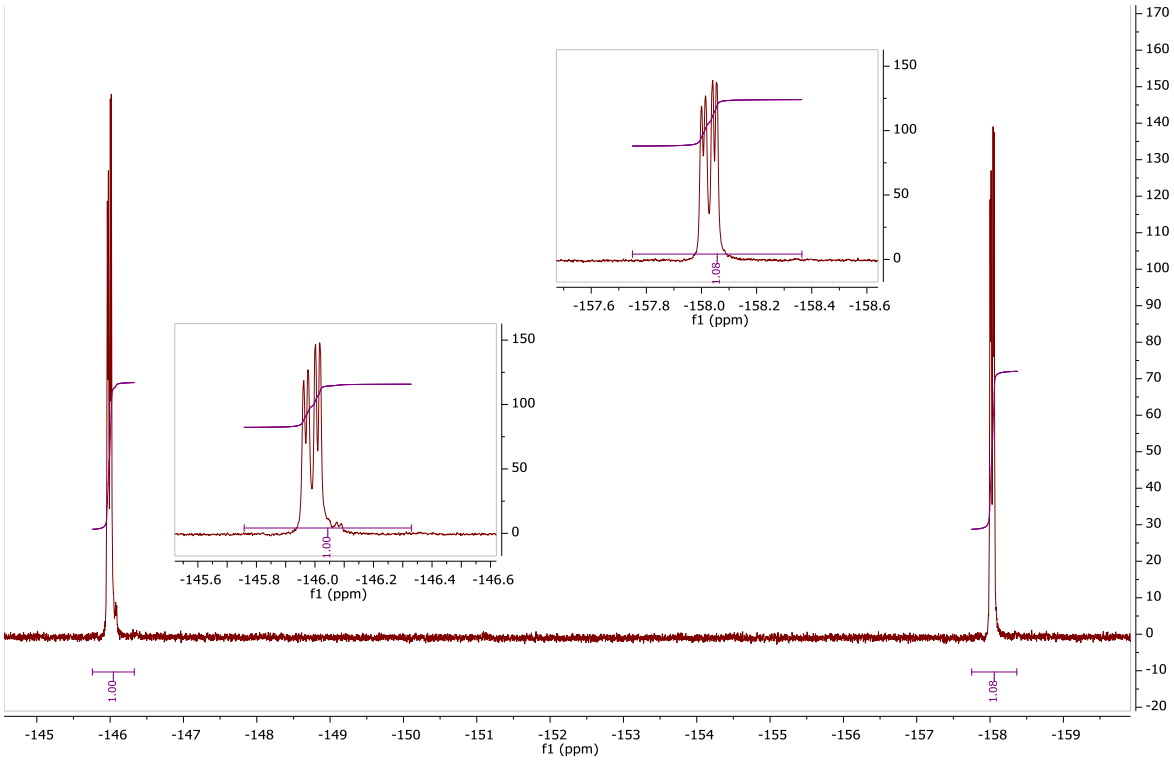

Figure S8. ^{19}F-NMR Spectrum of **AFF** in $CDCl_3$.

4. DSC Thermograms

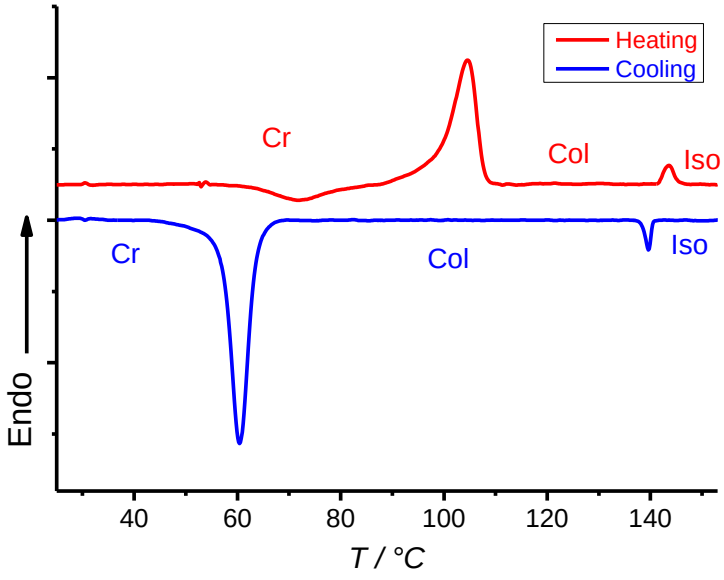

Figure S9. DSC traces of **AHH** with heating and cooling rates of 10 K/min^{-1}.

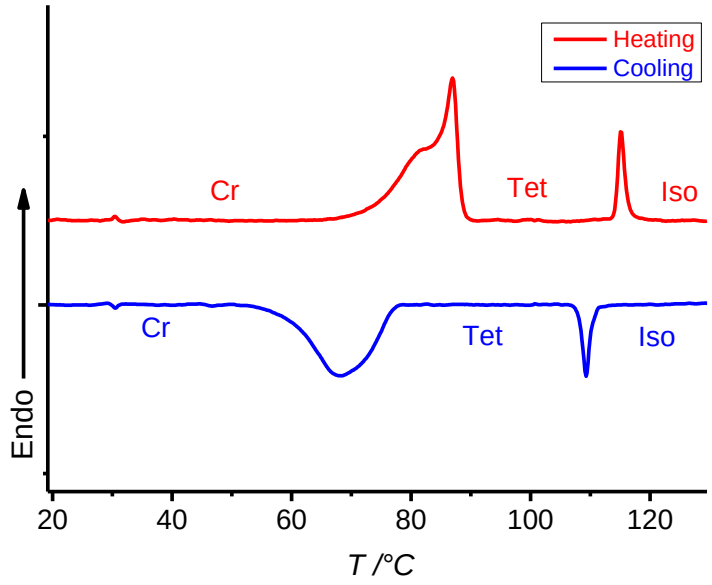

Figure S10. DSC traces of **AFH** with heating and cooling rates of 10 K/min^{-1}.

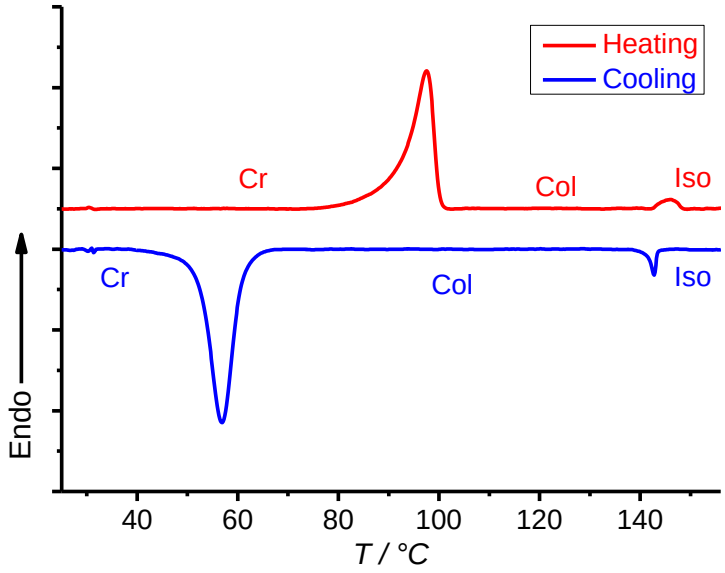

Figure S11. DSC traces of **AFF** with heating and cooling rates of 10 K/min^{-1}.

5. SAXS Data

Table S1. Experimental and calculated *d*-spacings, relative integrated intensities, and phases used in the reconstruction of electron densities for the *p6mm* hexagonal phase of **AHH** at 96 ºC upon cooling. All intensities are Lorentz and multiplicity corrected.

(hk)	$d_{obs.}$ (nm)	$d_{cal.}$ (nm)	*intensity*	*phase*
(10)	4.57	4.57	100.0	0
(11)	2.64	2.64	0.9	π
(20)	2.28	2.28	2.2	π
a = 5.27 nm				

Table S2. Experimental and calculated *d*-spacings, relative integrated intensities, and phases used in the reconstruction of electron densities for the *p6mm* hexagonal phase of **AFF** at 101 ºC upon cooling. All intensities are Lorentz and multiplicity corrected.

(hk)	$d_{obs.}$ (nm)	$d_{cal.}$ (nm)	*intensity*	*phase*
(10)	4.56	4.56	100.0	0
(11)	2.63	2.63	1.3	π
(20)	2.28	2.28	2.6	π
a = 5.27 nm				

Table S3. Experimental and calculated *d*-spacings, relative integrated intensities, and phases used in the reconstruction of electron densities for the $P4_2/mnm$ tetragonal phase of **AFH** at 96 ºC upon cooling. All intensities are Lorentz and multiplicity corrected.

(hkl)	$d_{obs.}$ (nm)	$d_{cal.}$ (nm)	*intensity*	*phase*
(110)	9.73	9.74	2.9	0
(200)	6.88	6.89	46.6	0
(101)	5.47	5.47	100	0
(111)	5.08	5.08	1.3	0
(310)	4.35	4.36	9.2	π
(211)	4.28	4.28	1.9	0
(221)	3.78	3.77	0.08	/
(301)	3.63	3.64	0.3	/
(311)	3.52	3.52	0.5	/

(400)	3.44	3.45	1.3	/
(410)	3.33	3.34	0.004	/
(321)	3.22	3.22	0.06	/
(420)	3.08	3.08	0.08	/
(002)	2.98	2.98	0.7	/
(411)	2.91	2.92	0.01	/
(331)	2.85	2.85	0.01	/
(112)				/
(202)	2.73	2.74	1.1	/
(212)	2.69	2.68	0.5	/
(222)	2.54	2.54	0.03	/
(511)	2.46	2.46	0.1	/
(312)				/
(521)	2.35	2.35	0.01	/
(322)				/
(412)	2.22	2.22	0.01	/
a = 13.78 nm; c = 5.96 nm				

Table S4. Summary of structural parameters.

Comp.	Phase	Lattice parameters/nm	V_{mol}/nm^3	V_{cell}/nm^3	n_{cell}	n_{raft}
AHH	*p6mm*	a = 5.27	2.313	10.82	5	5
AFH	$P4_2/mnm$	a = 13.78; b = 5.96	2.319	1131.74	546	5
AFF	*p6mm*	a = 5.27	2.325	10.82	5	5

V_{mol} was determined using the volume increments by Immirzi,[S5] $V_{cell} = 0.45*\sqrt{3}/2a^2$ for hexagonal lattice, $V_{cell} = a^2c$ for tetragonal cells, $n_{cell} = 0.893\cdot(V_{cell}/V_{mol})$, number of molecules within one unit cell, n_{raft} – number of molecules per raft in the columns.

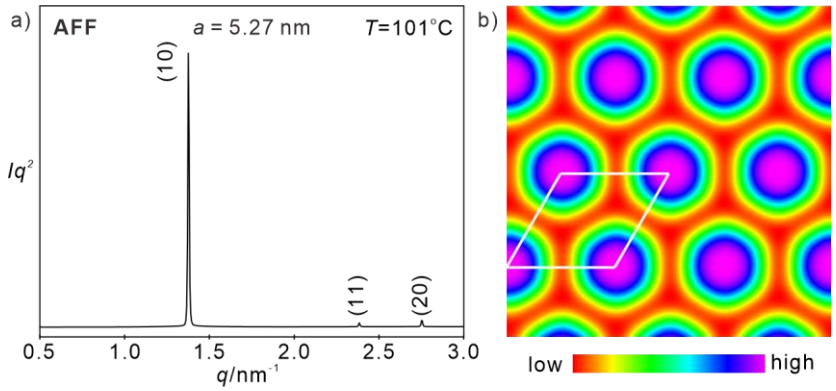

Figure S12. a) The SAXS diffractogram of **AFF** referring to the hexagonal columnar phase at 101 °C; b) the reconstructed ED map of the *p*6*mm* phase with white lines indicating the lattice.

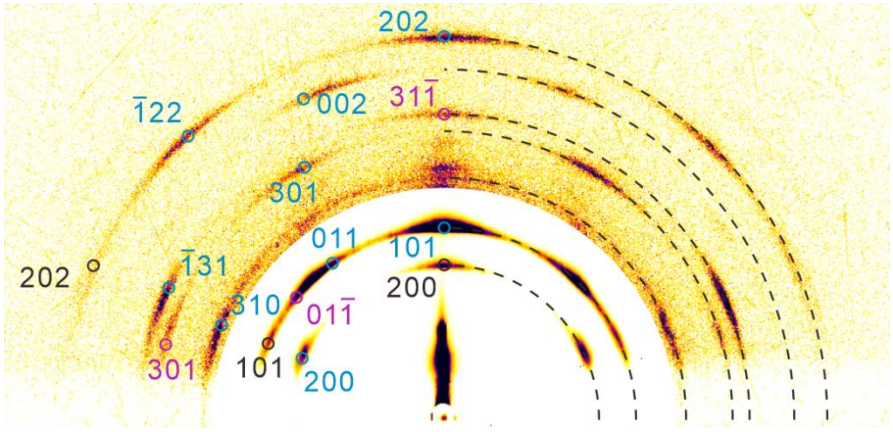

Figure S13. The GISAXS pattern of the aligned $P4_2/mnm$ phase formed by **AFH**. The tetragonal phase is aligned along three different directions, (200), (101), and $(31\bar{1})$. The nice fit between experimental data (arcs) and simulated position (circles) suggests that **AFH** forms a tetragonal phase.

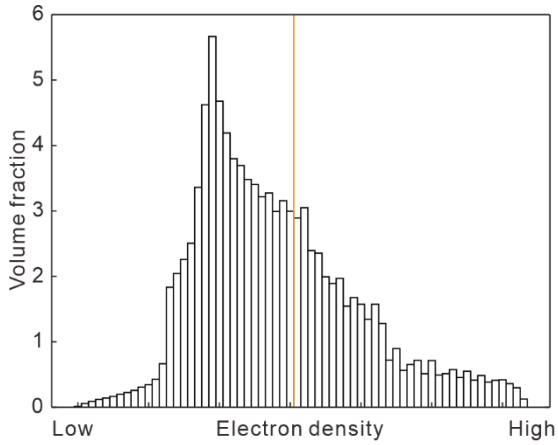

Figure S14. The electron density distribution histogram of the $P4_2/mnm$ phase formed by **AFH**. The yellow line indicates the boundary between aromatic core and aliphatic chains. The sharp and narrow distribution at the relatively low ED region indicates the good flexibility of aliphatic chains.

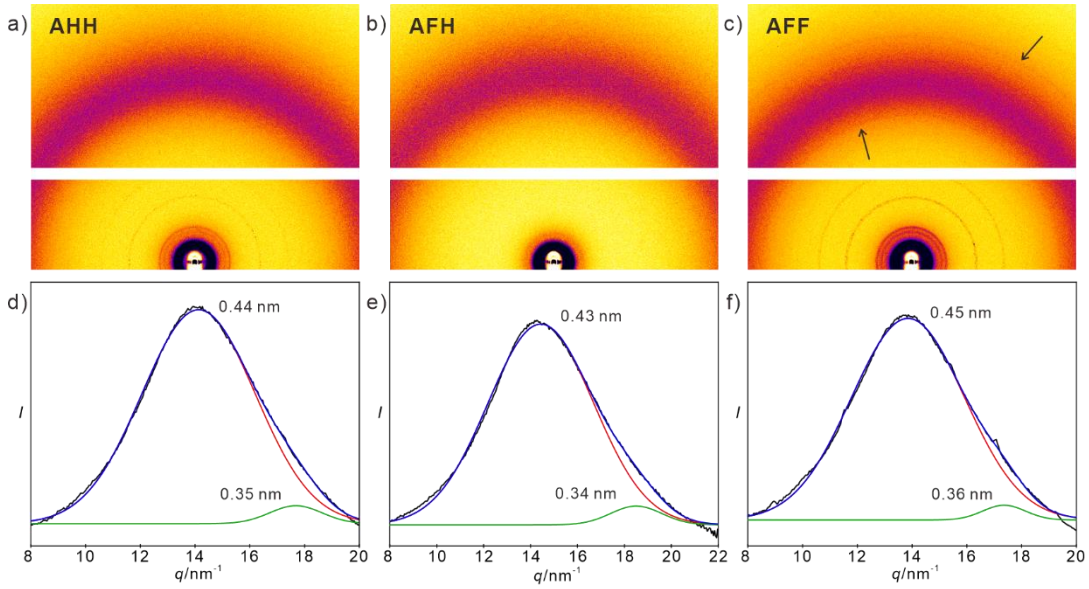

Figure S15. The WAXS pattern and 1D curves of (a, d) **AHH** at 120 °C ; (b, e) **AFH** at 100 °C, and (c, f) **AFF** at 120 °C. The interplay between polar interaction and the steric effect of core fluorination leads to the intermolecular distance shrinkage of **AFH** and expansion of **AFF**. Arrows in c) suggest the crystallization of **AFF**.

6. DFT Data

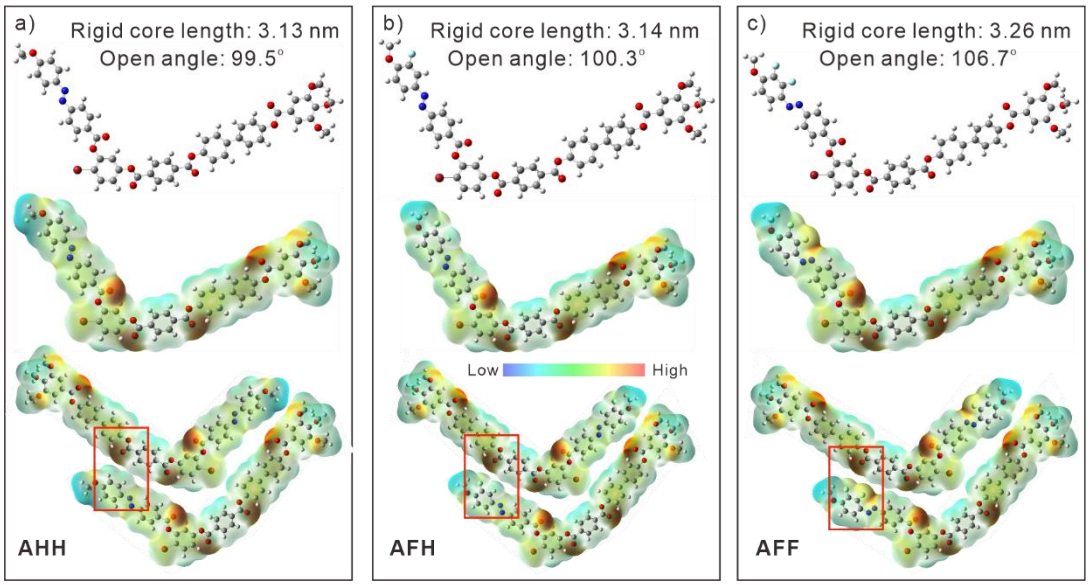

Figure S16. The DFT computation of molecular structure and electrostatic surface potential maps of (a) **AHH**; (b) **AFH,** and (c) **AFF**. The DFT computation was conducted by Gaussian09D1, visualized by Gaussview6 on the basis function of B3LYP/6-311G(d, p).

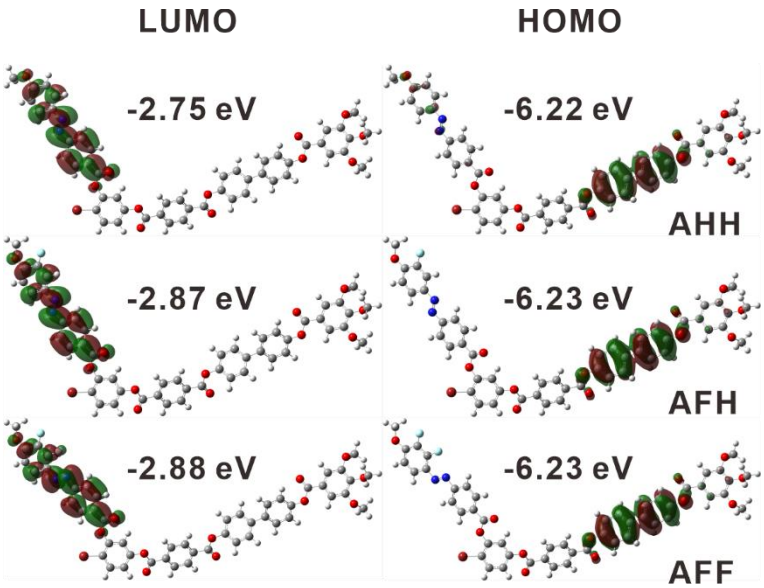

Figure S17. The DFT computation of HOMO/LUMO of **AHH**, **AFH**, and **AFF**.

7. Photoisomerization

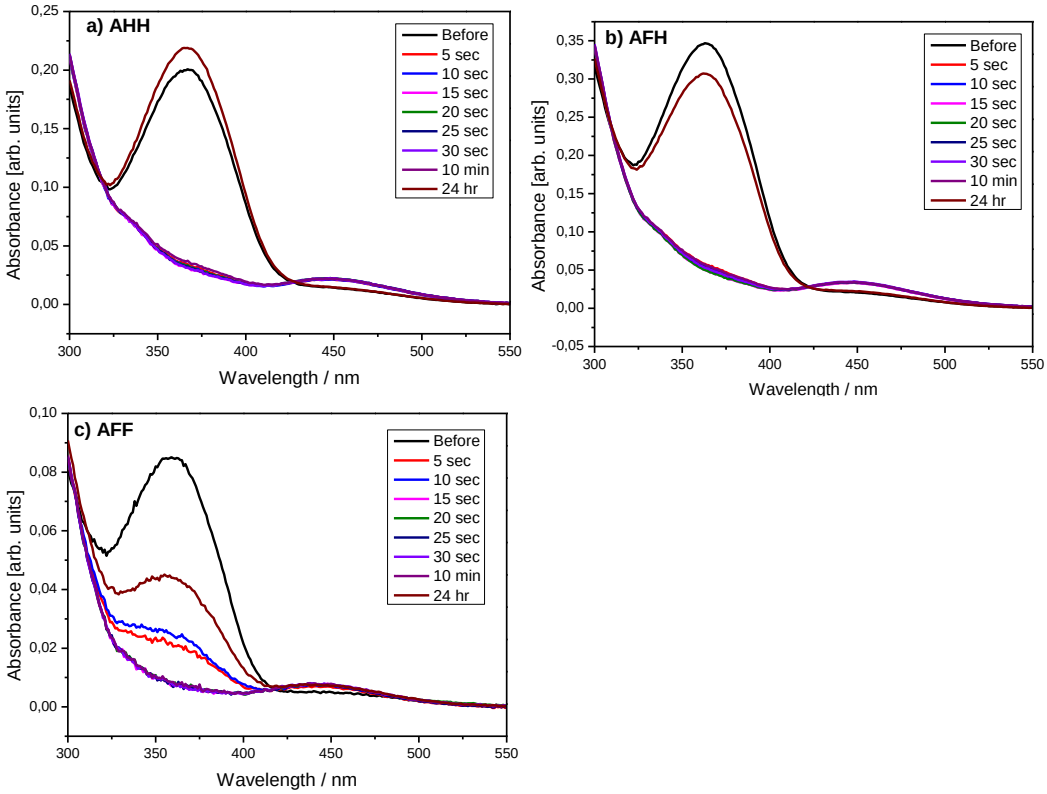

Figure S18. *Trans-Cis* photoisomerization under UV light irradiation for: a) **AHH**, b) **AFH**, and c) **AFF** dissolved in chloroform, as recorded at room temperature.

8. Charge transport studies via space charge limited current (SCLC) technique

The ITO and Au-coated glass plates, purchased from Ossila (U.K.), were cleaned via soap solution, acetone, and isopropyl alcohol (IPA). Subsequently, the surface treatment was also carried out using a UV Ozone Cleaner (Ossila, U.K.). The hole-only device composed of Glass/ITO/LC/Au was fabricated to assess hole mobility utilizing the space charge limited current (SCLC) technique **(**schematic shown in **Figure S19**).[S6,S7] The compounds **AHH**, **AFH**, and **AFF** were filled in the SCLC devices of thickness 9 µm (using Mylar spacers). During the measurements, the temperature of the devices was maintained using the Linkam LTS 350 hotplate connected with the Linkam TMS 94 with an accuracy of ± 0.1 °C. The current density-voltage (J/V) curves were recorded using Keysight B2902A Precision Source/Measure Unit (SMU). During the measurements, the temperature was controlled with an accuracy of ± 0.1 °C using the Linkam LTS 350 hotplate connected to a temperature controller Linkam TMS 94.

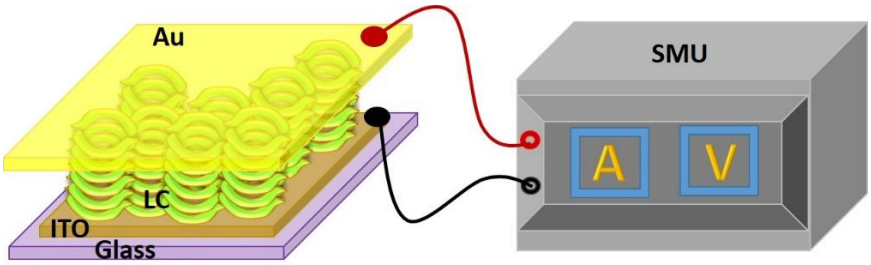

Figure S19. Schematic illustration of the SCLC hole-only device.

Assuming the negligible contribution of traps, the Mott−Gurney equation, shown below, can be used to determine the mobility:

$$J = \frac{9}{8}\varepsilon_o \varepsilon \mu \frac{V^2}{d^3} \qquad (1)$$

Where J is the current density, ε0 is the permittivity of free space, ε is the dielectric constant of the LC material, μ is the mobility, V is the voltage drop across the device, and *d* is the thickness of the LC material

9. Polarization measurements

Polarization measurements were carried out using the polarization current reversal method;[S8,S9] under which a triangular wave of 60 Hz and an externally applied field between 4-15 V/μm was employed. The value of polarization at different applied fields was determined by integrating the area of polarization reversal peak by using the formula :

$$P = \frac{1}{2A}\int i(t)dt \qquad (1)$$

Where, $\int i(t)dt$ Is the area under the current bump, and *A* is the active area (5 mm × 5 mm) of the liquid crystal (LC) cell.

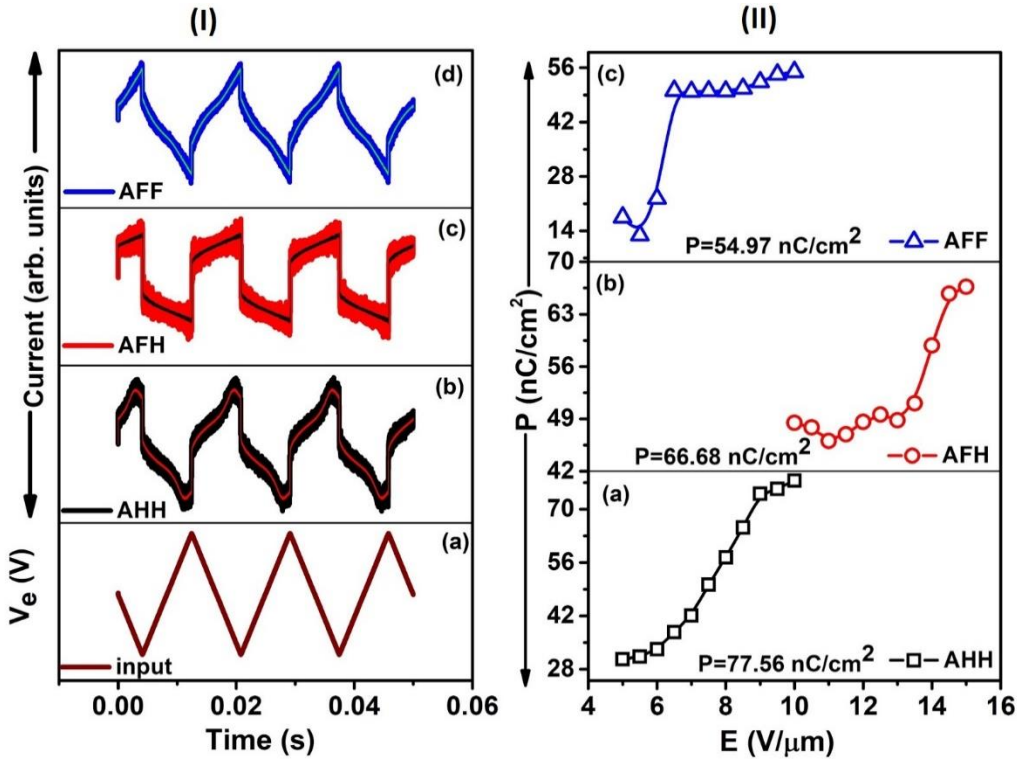

Figure S20. I(a) represents the input triangular wave signal of 60 Hz and 10 V/μm; whereas, I(b)-(d) show the polarization current reversal signal, using which the polarization values were determined. II(a)-(c) depict the variation of polarization of **AHH**, **AFH**, and **AFF** as a function of applied field at 100 °C.

10. References

S1. M. Alaasar, M. Prehm, C. Tschierske. *Chem. Eur. J.* **2016**, *22*, 6583.

S2. Q. Chang, W. Ding, S. Chen, K. Soundarajan, X. Cheng. *J. Mol. Liq.* **2022**, *363*, 119832.

S3. a) J.-S. Seo, Y.-S. Yoo, M.-G. Choi. *J. Mater. Chem.* **2001**, *11*, 1332; b) J. Matraszek, J. Mieczkowski, D. Pociecha, E. Gorecka, B. Donnio, D. Guillon. *Chem. Eur. J.* **2007**, *13*, 3377.

S4. M. Alaasar, M. Prehm, M. Brautzsch, C. Tschierske, *Soft Matter*, **2014**, *10*, 7285.

S5. A. Immirzi, B. Perini, *Acta Cryst.* **1977**, *A33*, 216.

S6. V. Bhat Subraya, D. P. Singh, F. Dubois, V. A. Raghunathan, A. Roy, S. Kumar, *ACS Appl. Electron. Mater.* **2024**, *6*, 8828.

S7. A. Patra, A. Shah, D. P. Singh, A. Roy, S. Kumar, *Chem. An Asian J.* **2024**, *19*, e202400542.

S8. R. Manohar, A. K. Srivastava, P. K. Tripathi, D. P. Singh, *J. Mater. Sci.* **2011**, *46*, 5969.

S9. D. P. Singh, S. K. Gupta, T. Vimal, R. Manohar, *Phys. Rev. E* **2014**, *90*, 022501.